

Title

Towards automated brain aneurysm detection in TOF-MRA: open data, weak labels, and anatomical knowledge

Authors

Tommaso Di Noto^a [0000-0002-5161-055X], Guillaume Marie^a [0000-0002-2447-1056], Sebastien Tourbier^a [0000-0002-4441-899X], Yasser Alemán-Gómez^{a,b} [0000-0001-6067-8639], Oscar Esteban^a [0000-0001-8435-6191], Guillaume Saliou^a [0000-0003-3832-7976], Meritxell Bach Cuadra^{a,c} [0000-0003-2730-4285], Patric Hagmann^a [0000-0002-2854-6561], Jonas Richiardi^a [0000-0002-6975-5634]

a. Department of Radiology, Lausanne University Hospital and University of Lausanne, Lausanne, Switzerland

b. Center for Psychiatric Neuroscience, Department of Psychiatry, Lausanne University Hospital and University of Lausanne, Lausanne, Switzerland

c. CIBM, Centre d'Imagerie BioMédicale, Lausanne, Switzerland

Information Sharing Statement – Data availability

Our open-access dataset is available on OpenNeuro under the CC0 license at <https://openneuro.org/datasets/ds003949>. The ADAM dataset can be downloaded from the challenge website <https://adam.isi.uu.nl/data/> after signing a confidentiality agreement. The code used for this study is available at https://github.com/connectomicslab/Aneurysm_Detection under the Apache-2.0 license.

Abstract

Brain aneurysm detection in Time-Of-Flight Magnetic Resonance Angiography (TOF-MRA) has undergone drastic improvements with the advent of Deep Learning (DL). However, performances of supervised DL models heavily rely on the quantity of labeled samples. To mitigate the recurrent bottleneck of voxel-wise label creation, we investigate the use of weak labels: these are oversized annotations which are considerably faster to create. We present a deep learning algorithm for aneurysm detection that exploits weak labels during training. In addition, our model leverages prior anatomical knowledge by focusing only on plausible locations for aneurysm occurrence. We created a retrospective dataset of 284 TOF-MRA subjects (170 females) out of which 157 are patients (with 198 aneurysms), and 127 are controls. Our open TOF-MRA dataset, the largest in the community, is released on OpenNEURO. To assess model generalizability, we participated in a challenge for aneurysm detection with TOF-MRA data (93 patients, 20 controls, 125 aneurysms). Weak labels

were 4 times faster to generate than their voxel-wise counterparts. When using prior anatomical knowledge, our network achieved a sensitivity of 80% on the in-house data, with False Positive (FP) rate of 1.2 per patient. On the public challenge, sensitivity was 68% (FP rate = 2.5), ranking 4th/18 on the open leaderboard. We found no significant difference in sensitivity between aneurysm risk-of-rupture groups ($p = 0.75$), locations ($p = 0.72$), or sizes ($p = 0.15$). Our code is made available for reproducibility.

Keywords: Model robustness - Weak annotation - Domain knowledge - Deep Learning - Magnetic Resonance Angiography – Aneurysm detection.

Main Body

1 - Introduction

Time-Of-Flight Magnetic Resonance Angiography (TOF-MRA) is a non-invasive and non-contrast imaging technique sensitive to the blood flow in brain vessels. TOF-MRA has found widespread clinical application to identify Unruptured Intracranial Aneurysms (UIAs) which are small (typical diameter $\cong 5\text{mm}$) abnormal focal dilatations in cerebral arteries (Chen et al., 2018). If untreated, UIAs can rupture and lead to subarachnoid hemorrhages which have a mortality rate of 40% and usually cause severe disability for patients (Frösen et al., 2012).

Radiologists detect aneurysms by selectively scrolling through the TOF-MRA volumes in different planes - for instance, they check in the axial plane the most recurrent locations where aneurysms can occur. Then, the sagittal view permits better views of areas like the basilar trunk; afterwards, the coronal view can be used for areas like the anterior cerebral arteries or the Sylvian segments. In addition, Maximum Intensity Projection (MIP) images can be used to search for stenoses, or to confirm potential aneurysms that were spotted.

Considering that the workload of radiologists is steadily increasing (Rao et al., 2021) and the detection of UIAs is a meticulous and non-trivial task (Nakao et al., 2018), the development of automated algorithms that aid clinicians in detecting aneurysms with high sensitivity is an active line of research which holds the promise of improving care while reducing radiologists' assessment times.

Several automated methods that address automated UIA detection have been proposed before the advent of Deep Learning (DL). For instance, (X. Yang et al., 2011) used candidate points of interest in the brain arteries to locate aneurysms. In another work, (Arimura, Li, Korogi, Hirai, & Abe, 2004) tried to detect aneurysms via an enhancement of the MRA images followed by a custom thresholding to identify aneurysm candidates, and a final classification of the candidates.

Then, starting from 2016, there was a shift towards DL algorithms, which have now become the de facto standard for UIA detection. Table 1 illustrates several recent studies that use DL for UIA detection. Despite their success, these DL approaches are still constrained by a major bottleneck common to several medical applications: the lack of large, labeled datasets. This is mainly due to two factors: first, the creation of voxel-wise labels for medical images is tedious and time-consuming for radiologists (Razzak, Naz, & Zaib, 2018); second, none of the TOF-MRA studies to date made their dataset publicly available (Joo et al., 2020; Nakao et al., 2018; Sichtermann et al., 2019; Stember et al., 2019; Ueda, Doishita, & Choppin, 2019). This hampers reproducibility and multi-site analyses that are paramount for building robust DL architectures. In addition, none of the related studies evaluated their models on the openly available TOF-MRA challenge dataset (Timmins et al., 2021), thus hindering fair comparisons of detection results.

In this work, we develop a fully automated DL network for UIA detection and propose to mitigate the data availability bottleneck as follows: we explore the use of “weak” labels (Abousamra et al., 2020; Ezhov, Zakirov, & Gusarev, 2018; Ke, Bugeau, Papadakis, Schuetz, & Schönlieb, 2020). These can be coarse or oversized annotations that are less precise, but considerably faster to create for medical

experts. In addition, we release our annotated dataset to the community. To the best of our knowledge, this will be the largest openly available TOF-MRA aneurysm dataset to date.

Furthermore, we assess multi-site robustness by evaluating of our algorithm on the external TOF-MRA challenge dataset (Timmins et al., 2021). Last, we constrain the DL analysis only to the areas of the brain where aneurysm occurrence is plausible. This anatomically-informed approach aims at simulating the selective analysis that radiologist perform on the TOF-MRA scans.

Table 1: summary of papers that use deep learning models to tackle automated brain aneurysm detection/segmentation. MRA: Magnetic Resonance Angiography; CTA: Computed Tomography Angiography; DSA: Digital Subtraction Angiography; N = number; Sub = subjects; DL = Deep Learning

Paper	Modality	Task(s)	N. Sub	N. Aneurysms	DL Model	Model input	Voxel-wise labels	Multi-Site
(Ueda et al., 2019)	MRA	Detection	1271	1477	ResNet	2D patches	Not specified	Yes
(Joo et al., 2020)	MRA	Detection	744	761	3D ResNet	3D patches	Yes	Yes
(Nakao et al., 2018)	MRA	Detection	450	508	CNN	2D MIP patches	Yes	No
(Stember et al., 2019)	MRA	Detection	302	336	RCNN	2D MIP patches	Yes	No
(Sichtermann et al., 2019)	MRA	Detection (via segmentation)	85	115	DeepMedic	3D patches	Yes	No
(Shi et al., 2020)	CTA	Detection + Segmentation	1177	1099	3D UNET	3D patches	Yes	Yes
(J. Yang et al., 2020)	CTA	Detection	1068	1337	ResNet	3D patches	Not specified	Yes
(Park et al., 2019)	CTA	Segmentation + CAD assessment	662	358	HeadXNet	3D patches	Yes	No
(Dai et al., 2020)	CTA	Detection	311	352	RCNN	2D NP images	Not specified	Yes
(Liu et al., 2021)	DSA	Detection + Segmentation	451	485	3D UNET	3D DSA volumes	Yes	No
(Duan et al., 2019)	DSA	Detection	281	261	2D CNN	2D DSA images	Bounding Boxes	No
(Hainc et al., 2020)	DSA	Detection	240	187	2D CNN	2D DSA images	ROI circle	No

2 - Materials and Methods

2.1 Dataset

This study was approved by the regional ethics committee; written informed consent was waived. In this retrospective work, we included consecutive patients that underwent TOF-MRA between 2010

and 2015, and for which the corresponding radiological reports were available. Patients with ruptured/treated aneurysms or with other vascular pathologies were excluded. Totally thrombosed aneurysms and infundibula (dilatations of the origin of an artery) were likewise excluded. In total, we retrieved 284 TOF-MRA subjects: 156 had one (or more) UIAs, while 127 did not present any. Table 2 illustrates the main demographic information for our study group. A 3D gradient recalled echo sequence with Partial Fourier technique was used for all subjects (acquisition parameters are reported in Online Resources - Table 1). 214 subjects of this study were also used in (Di Noto et al., 2020). This prior article dealt with patch-wise classification, whereas here we address patient-wise aneurysm detection.

Table 2. Demographics of the study sample. Patients = subjects with aneurysm(s). Controls = subjects without aneurysms. Age calculated in years and presented as mean \pm standard deviation. N=number of samples; M = males; F = females. Two-sided t-test to compare age between patients and controls. Chi-squared test to compare sex counts between patients and controls.

	Patients	Controls	Test, <i>p</i> value	Whole Sample
N	157	127	/	284
Age (y)	56 \pm 14	46 \pm 17	$t = -4,3, p = 7.6 \times 10^{-7}$	51 \pm 16
Sex	53M, 104F	61M, 66F	$\chi^2 = 5.9 p = 0.01$	114M, 170F
# Aneurysms	198	0	/	198

Aneurysms were annotated by one radiologist with 2 years of experience in neuroimaging, and double-checked by a senior neuroradiologist with over 15 years of experience to exclude potential false positives or false negatives. Two annotation schemes were followed:

1. **Weak labels:** for most subjects (246/284), the radiologist used [Mango](#) (v. 4.0.1) to create the aforementioned weak labels. These correspond to spheres that enclose the whole aneurysm, regardless of the shape. A visual example of one weak label is provided in Figure 1.
2. **Voxel-wise labels:** for the remaining 38 subjects, the radiologist used [ITK-SNAP](#) (v. 3.6.0) (Yushkevich et al., 2006) to create voxel-wise labels drawn slice by slice scrolling in the axial plane. No specific selection criterion was used to select the 38 subjects, which were consecutive to the 246 of the first group.

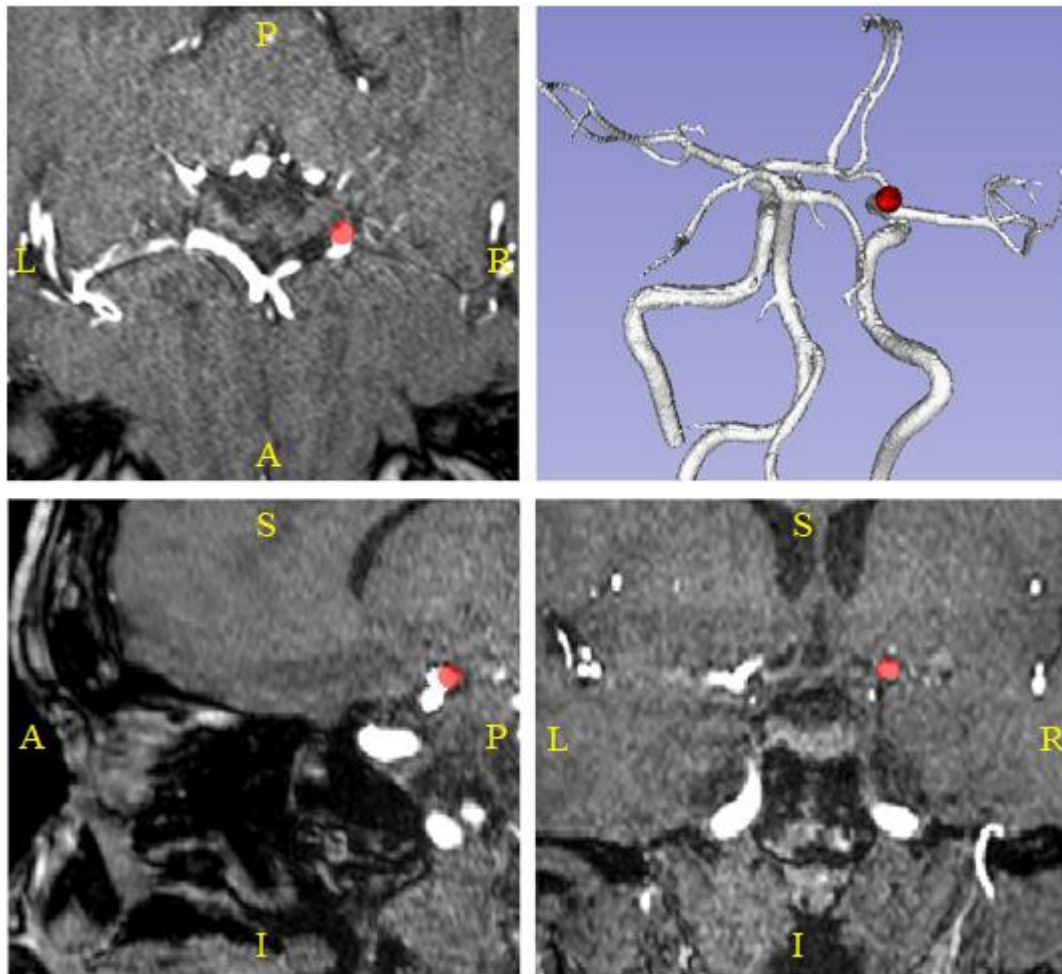


Fig. 1 TOF-MRA orthogonal views of a 62-year-old female patient. Red areas correspond to our spherical weak labels. Top-left: axial plane; top-right: 3D posterior reconstruction of the cerebral arteries; bottom-left: sagittal plane; bottom-right: coronal plane

We selected a subset of 14 patients (mean aneurysm size (s.d.) = 5.2 (1.0) mm) to assess the time difference between the two annotation schemes.

The overall number of aneurysms included in the study is 198 (178 saccular, 20 fusiform). Table 3 shows their locations and sizes grouped according to the PHASES score (Greving et al., 2014). This is a clinical score used to assess the 5-year risk of rupture of aneurysms.

Table 3. Locations and sizes of aneurysms according to the PHASES score for the in-house dataset. ICA = Internal Carotid Artery, MCA = Middle Cerebral Artery, ACA = Anterior Cerebral Arteries, Pcom = Posterior communicating artery, Posterior = posterior circulation. d = maximum diameter.

		Count	%
Location	ICA	59	29.8 (59/198)
	MCA	57	28.8 (57/198)
	ACA/Pcom/Posterior	82	41.4 (82/198)
Size	$d \leq 7 \text{ mm}$	180	91.0 (180/198)
	$7 - 9,9 \text{ mm}$	7	3.5 (7/198)
	$10 - 19,9 \text{ mm}$	10	5.0 (10/198)
	$d \geq 20 \text{ mm}$	1	0.5 (1/198)

In addition, for post-hoc analysis and stratification purposes, we divided the aneurysms into two groups based on their risk of rupture: *low-risk* and *medium-risk*. Aneurysms in the *low-risk* group are those that are monitored over time, but do not require any intervention. Instead, aneurysms in the *medium-risk* group can be considered for treatment. We computed for each aneurysm a partial PHASES score that only considered size, location, and patient's age, thus neglecting population, hypertension, and earlier aneurysmal hemorrhage, since this information was not available for all patients. If an aneurysm had partial PHASES score ≤ 4 , it was assigned to the *low-risk* group, while if it had a partial score > 4 , it was assigned to the *medium-risk* group. Each aneurysm was reviewed by our senior neuroradiologist to assess whether the partial PHASES score was reasonable. Fusiform aneurysms were excluded from the risk analysis since the PHASES score was built for saccular aneurysms. Similarly, extracranial carotid artery aneurysms were excluded since they do not bleed in the subarachnoid space. This resulted in 141 *low-risk* and 23 *medium-risk* aneurysms. A table summarizing aneurysm shape, size, location, associated PHASES score and risk groups is provided in the Online Resources.

The dataset was anonymized and organized according to the Brain Imaging Data Structure (BIDS) standard (Gorgolewski, 2008). It is available on OpenNeuro (Markiewicz et al., 2021) at <https://openneuro.org/datasets/ds003949> under the CC0 license.

ADAM dataset - To evaluate model performances in data coming from a different institution, we participated to the Aneurysm Detection And segmentation (ADAM) challenge (<http://adam.isi.uu.nl/>) (Timmins et al., 2021). The ADAM training dataset is composed of 113 TOF-MRA (93 patients with UIAs, 20 controls). The total number of UIAs is 125 and the voxel-wise annotations were drawn in the axial plane by two radiologists. Instead, the unreleased test dataset is made of 141 cases (117 patients, 26 controls) and it is solely used by the organizers to compute patient-wise results.

2.2 Data processing

Several preprocessing steps were carried out for each subject. First, we performed skull-stripping with the FSL Brain Extraction Tool (v. 6.0.1) (Smith, 2002). Second, we applied N4 bias field correction with SimpleITK (v. 1.2.0) (Tustison et al., 2010). Third, we resampled all volumes to a median voxel spacing, again with SimpleITK. This effectively normalizes nonuniform voxel sizes (Isensee, Jaeger, Kohl, Petersen, & Maier-Hein, 2021). Last, a probabilistic vessel atlas built from multi-center MRA datasets (Mouches & Forkert, 2014) was co-registered to each patient's TOF-MRA using ANTS (v. 2.3.1) (Avants, Tustison, & Johnson, 2014) (details in Online Resources – Section A). The atlas was used both during patch sampling (see section 2.3), and inference (see section 2.5).

2.3 Anatomically-informed patch sampling

A patch-based approach was adopted during training: we used 3D patches as input to our network. We apply an anatomically-informed selection of patches, as the task of aneurysm detection is extremely spatially constrained: we exploit the prior information that aneurysms a) must occur in vessels, and b) tend to occur in precise locations of the vasculature. To include this strong anatomical knowledge, one of our radiologists pinpointed in the vessel atlas (section 2.2) the location of 20 landmark points where aneurysm occurrence is most frequent (list in Online Resources - Table 2). These points were chosen according to the literature (Brown & Broderick, 2014) and were co-registered to the TOF-MRA space of each subject, as illustrated in Figure 2.

To create the training dataset, we extracted both negative (without aneurysms) and positive (with aneurysms) patches. Specifically, 8 positive patches per aneurysm were randomly extracted in a non-centered fashion. Then, we extracted 50 negative patches per TOF-MRA volume. Out of these, 20 were centered in correspondence with the landmark points, 20 were patches containing vessels (details in Online Resources – Section B), and 10 were extracted randomly. Overall, this sampling strategy allows us to extract most of the negative patches (i.e., all but the random ones) which are comparable to the positive ones in terms of average intensity. To mitigate class imbalance, we applied data augmentations on positive patches: namely, rotations (90° , 180° , 270°), flipping (horizontal, vertical), contrast adjustment, gamma correction, and addition of gaussian noise.

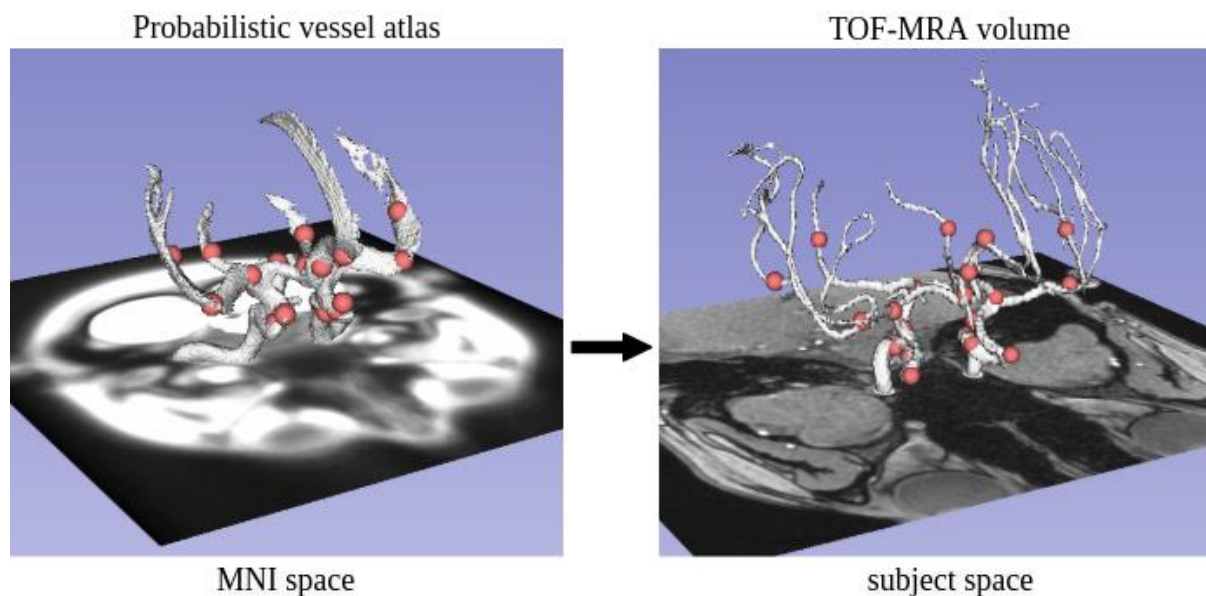


Fig. 2 (left): 20 landmark points (in red) located in specific positions of the cerebral arteries (white segmentation) in MNI space. **(right):** same landmark points co-registered to the TOF-MRA space of a 21-year-old, female subject without aneurysms

2.4 Network architecture

The deep learning model used in this study is a custom 3D UNET, inspired by the original work (Özgün, Abdulkadir, Lienkamp, Brox, & Ronneberg, 2016). We used upsample layers in the decoding branch rather than transpose convolutions since these led to faster model convergence. Figure 3 illustrates the structure of our network. We set the side of the input patches to $64 \times 64 \times 64$ voxels to include even the largest aneurysms. All patches were Z-score normalized, as is common practice

(Bengio, Goodfellow, & Courville, 2016). A kernel size of $3 \times 3 \times 3$ was used in all convolutional layers, with padding and stride=1.

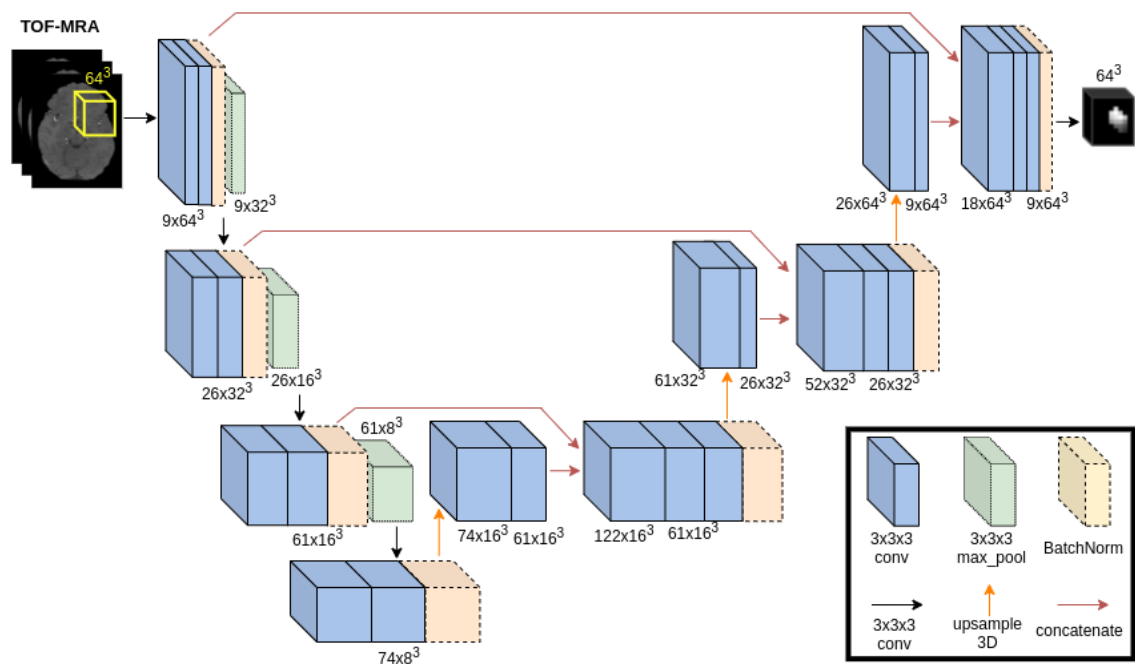


Fig. 3 Proposed variant of the 3D UNET. The input corresponds to a $64 \times 64 \times 64$ voxels TOF-MRA patch. The output is a probabilistic patch with the same size of the input, but where each voxel corresponds to the probability of either belonging to foreground (i.e., aneurysm) or background. Conv = convolutional; Max_pool = max pooling; BatchNorm = batch normalization

We applied the ReLU activation function for all layers, except for the last layer which is followed by a sigmoid function. To fit the model, the Adam optimization algorithm (Kingma & Ba, 2015) was applied with adaptive learning rate (initial learning rate = 0.0001). We trained the model for 100 epochs, and we adopted the Combo loss function (Taghanaki et al., 2019) with $\alpha = \beta = 0.5$. This function combines Dice and Cross-entropy, and has proven to be effective for imbalanced segmentation tasks. We used Xavier initialization (Glorot & Bengio, 2010) for all layers. Biases were initialized to 0 and a batch size of 8 was chosen. Batch normalization (Ioffe & Szegedy, 2015) was used to prevent overfitting. The number of convolutional filters, the batch size, the value of α (and therefore $\beta=1-\alpha$) and the learning rate were chosen using the Optuna algorithm (Akiba, Sano, Yanase, Ohta, & Koyama, 2019) on an internal validation set (20% of training cases of external fold 1). The total number of trainable parameters in our network is 855,111. Training and evaluation were performed with Tensorflow 2.4.0 and a GeForce RTX 2080TI GPU with 11GB of SDRAM.

2.5 Patient-wise evaluation

To evaluate detection performances, we conducted a 5-fold cross-validation. The patches extracted from the training subjects (80%) were used for fitting the model, while the test subjects (20%) were used to compute patient-wise results. To avoid over-optimistic results, we ensured that patients with multiple sessions were not split between training and test set.

Anatomically-informed sliding-window - The patient-wise evaluation was performed following the sliding-window approach (details in Online Resources – Section C). We exploited again the prior anatomical information described in section 2.3 by retaining only the patches which are both within a minimum distance from the landmark points and fulfill specific intensity criteria (details in Online Resources – Section B). The rationale behind this choice was to only focus on patches located in the main cerebral arteries, as shown in Figure 4. Two post-processing expedients were adopted: first, we kept a maximum of 5 candidate aneurysms per patient (only the 5 most probable). Second, we applied test-time augmentation to increase sensitivity.

2.6 Evaluation methods

We evaluated our model on two datasets. First, we computed cross-validated detection results for our in-house data to assess the effectiveness of weak labels and of the use of prior anatomical information. Second, we tested our model on the ADAM dataset to evaluate generalizability. In line with ADAM, we used sensitivity and false positive (FP) rate as detection metrics. A detection was considered correct if the center-of-mass of the predicted aneurysm was located within the maximum aneurysm size of the ground truth mask. In addition, we computed the Free-response Receiver Operating Characteristic (FROC) curve (Chakraborty & Berbaum, 2004). To compare different model configurations (section 3.1), we used a two-sided Wilcoxon signed-rank test of the areas under the FROC curves across test subjects, as similarly performed in (Ward, Naik, Guthrie, Wilson, & Robinson, 1999). To compare the performances of a configuration with respect to aneurysm rupture risk, location and size (section 3.3) we performed several Chi-squared tests (McHugh, 2012).

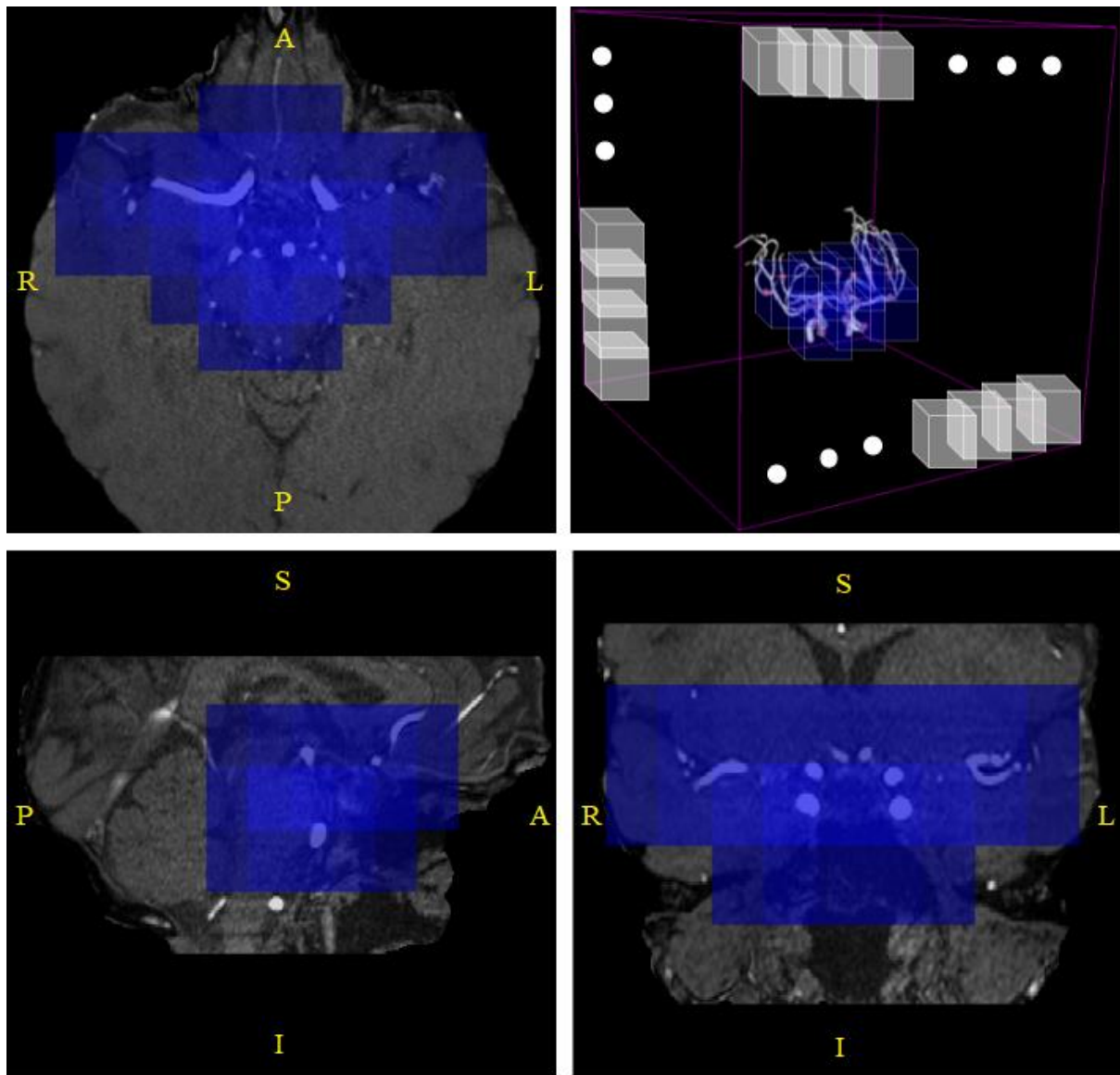


Fig. 4 TOF-MRA orthogonal views of a 62-year-old female subject after brain extraction: blue patches are the ones which are retained in the *anatomically-informed* sliding-window approach. (top-right): 3D schematic representation of sliding-window approach; out of all the patches in the volume (white patches), we only retain those located in the proximity of the main brain arteries (blue ones)

The statistical tests were performed using SciPy (v.1.4.1), setting a significance threshold $\alpha=0.05$.

In summary, the following experiments were conducted:

1. We compared the anatomically-informed approach with a baseline where no anatomical information is used.

2. We assessed the difference between weak and voxel-wise labels in terms of annotation time and detection performance by adding 38 patients with voxel-wise labels, and adding the same patients with ‘weakened’ labels.
3. We stratified results with respect to aneurysm risk-of-rupture, location, and size.
4. We evaluated performances on the ADAM test dataset.

The code used for this study is available on https://github.com/connectomicslab/Aneurysm_Detection, together with the configuration files to replicate all the experiments, and the weights of the trained model if users simply want to perform inference.

3 - Results

3.1 Anatomical information increases detection performances

In the baseline model, all non-zero patches of the TOF-MRA volumes are retained in the sliding-window approach, thus disregarding any anatomical constrain. Rows 1 and 3 of Table 3 illustrate detection performances of the baseline and of the anatomically-informed model with voxel-wise labels, respectively. The anatomically-informed (row 3) achieved higher detection results (sensitivity=80%, FP rate=1.2) and statistically outperformed the anatomically-agnostic baseline (two-sided Wilcoxon signed-rank test on the areas Under the FROC curves, $W = 0.0$, $p = 6 \times 10^{-11}$).

Table 3. Average detection results on the in-house dataset across test folds. Sensitivity values are reported as mean and 95% Wilson confidence interval inside parentheses. Avg = average; FP = false positive; CI = confidence interval; Baseline = non anatomically-informed. Voxel-wise = labels drawn slice by slice on the axial plane; Weakened = voxel-wise labels that are artificially converted to weak spherical labels. Subs = subjects.

	Model	Labels of 38 added subs	Avg. Sensitivity (CI)	Avg. FP rate
1	Baseline	Voxel-wise	61/127 = 48% (38%, 55%)	4.8
2	Anatomically-Informed	Weakened	95/127 = 75% (65%, 80%)	1.3
3	Anatomically-Informed	Voxel-wise	101/127 = 80% (72%, 85%)	1.2

To provide a visual interpretation of our network predictions, we show in Figure 5 one correctly identified aneurysm (true positive), one small, missed aneurysm (false negative) and one false positive prediction.

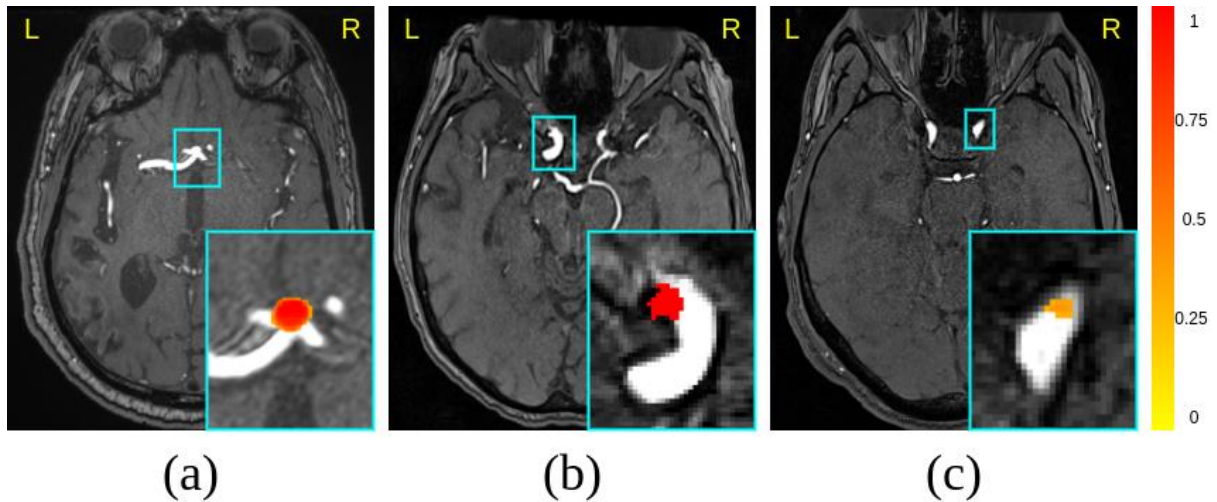


Fig. 5 Qualitative analysis of predictions and errors. The heatmap generated by the network ranges from 0 (low probability, yellow color) to 1 (high probability, red color) (a) True positive prediction in the anterior communicating artery. (b) False negative (i.e., missed aneurysm) in the internal carotid artery, The ground truth label mask is shown in red. (c) False Positive prediction in the internal carotid artery

3.2 Weak labels allow 4-fold annotation speedup without degrading performances

There was a significant difference in the time needed to create weak annotations (23 seconds \pm 6 per aneurysm), compared to voxel-wise annotations (93 seconds \pm 25) (two-sided Wilcoxon signed-rank test – annotation timings, $W=0$, $p = 0.001$), resulting in an approximately 4-fold speedup.

To evaluate the effect of annotation quality, for the 38 subjects with voxel-wise labels we artificially generated the corresponding weak spherical labels (*weakened* labels, details in Online Resources – Section D). Detection results with *weakened* labels are shown in row 2 of Table 3. The configuration with voxel-wise labels (row 3) had higher sensitivity and lower FP rate. However, this difference was not significant (two-sided Wilcoxon signed-rank test on the areas under the FROC curves, $W = 14.0$, $p = 0.054$).

Figure 6 illustrates the FROC curves corresponding to the models of Table 3. As shown by the Wilcoxon tests, the anatomically-informed model with voxel-wise labels (green curve) outperforms

the baseline (red curve) at all operating points. The confidence intervals of the two anatomically-informed models (green and blue curves) overlap, thus indicating that performances are statistically comparable.

3.3 The proposed network ranked 4th /18 in an independent benchmark on a held-out dataset

Table 4 illustrates detection results on the ADAM test dataset. Our algorithm ranked in 4th/18 position for detection and in 4th/15 position for segmentation (with highest volumetric similarity). Interested readers can check the methods proposed by other teams on the challenge website (<https://adam.isi.uu.nl/>) and in the paper (Timmins et al., 2021).

Table 4. Detection results on the ADAM dataset. Our team (in bold) ranked in 4th position in the open leaderboard out of 18 participating groups. Sens = sensitivity, FP = false positive.

Ranking	Team	Detection	
		Sens.	Avg. FP rate
1	abc	68%	0.40
2	xlim	70%	4.03
3	mibaumgartner	67%	0.13
4	unil-chuv3	68%	2.50
5	joker	63%	0.16
...			
18	ibbm	2%	0.01

3.4 Detection performances are robust across rupture risk, location, and size

Supplementary Figure 1 (see Online Resources) illustrates performances achieved by our top-performing model (row 3, Table 4) stratified according to the two risk groups presented in section 2.1. For the *low-risk* group, our model reaches a mean sensitivity of 80%, while for the *medium-risk* group it reaches a mean sensitivity of 73%. The difference was not significant ($\chi^2 = 0.09$, $DoF = 1$, $p = 0.75$). In Supplementary Figures 2 and 3, we also report the model sensitivity stratified according to aneurysm location and size, respectively. No significant difference was found across different locations ($\chi^2 = 0.64$, $DoF = 2$, $p = 0.72$) or sizes ($\chi^2 = 0.92$, $DoF = 2$, $p = 0.15$, excluding n=1 huge aneurysm with $s > 20$ mm).

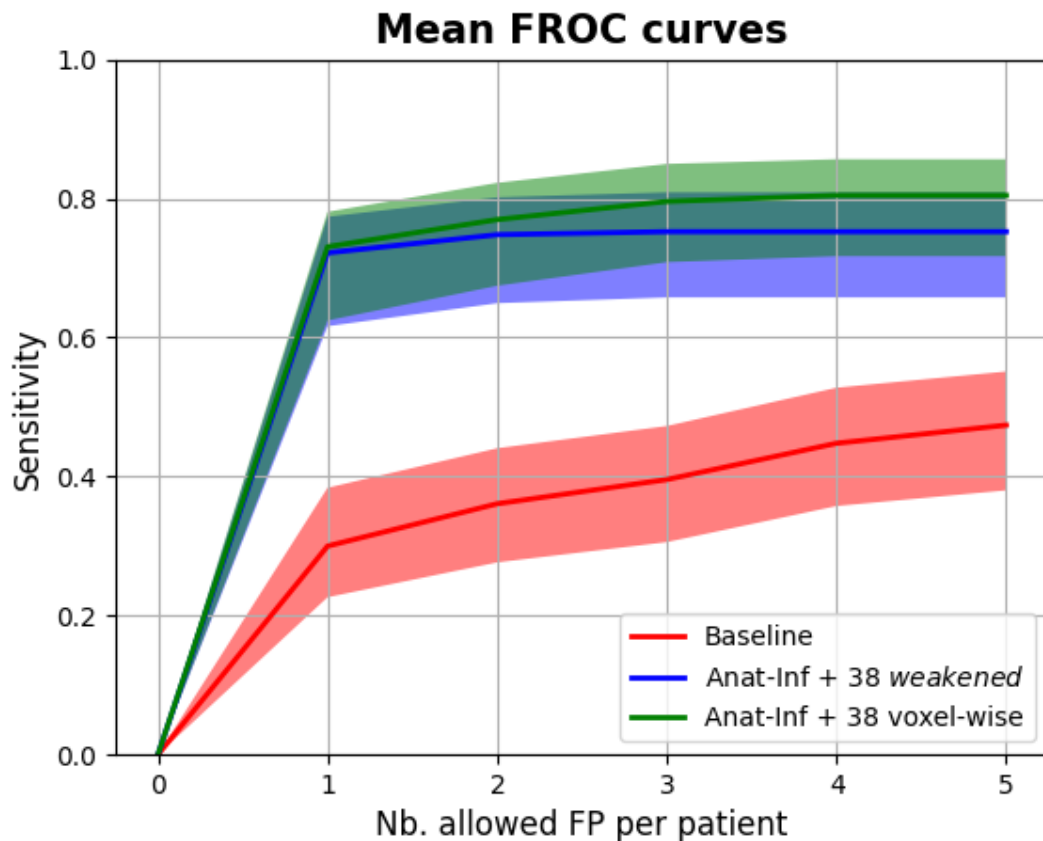


Fig. 6 Mean Free-response Receiver Operating Characteristic (FROC) curves across the five test folds of the cross-validation. Shaded areas represent the 95% Wilson confidence interval. The three models correspond to those presented in Table 3. Baseline: anatomically-agnostic model; Anat-Inf = Anatomically-Informed

4 - Discussion

This work shows that competitive results can be obtained in automated aneurysm detection for TOF-MRA data even with rapid data annotation. To this end, we proposed a fully-automated, deep learning algorithm that is trained using weak labels and exploits prior anatomical knowledge.

Despite being less accurate, weak labels are drastically faster to create for medical experts reducing fourfold the annotation time. Although the configuration with voxel-wise labels (Row 3, Table 4) had higher detection results, we found no statistical difference when comparing with the configuration with *weakened* labels (Row 2, Table 4). This finding indicates that weak labels are sufficient to obtain satisfactory detection results on our in-house dataset. If reasoning in terms of larger datasets (e.g.,

thousands of patients), the weak annotation proposed in this work is a scalable solution which can significantly alleviate the annotation bottleneck in medical ML applications.

In addition to the use of weak labels, our model leverages the underlying anatomy of the brain vasculature (i.e., we “*anatomically-informed*” our network) in order to simulate the radiologists’ exploration of the TOF-MRA scans. First, most of the negative patches extracted during training either contained a vessel or were located in correspondence with the aneurysm landmark points. Second, we limited the sliding-window approach only to regions of the brain that are plausible for aneurysm occurrence. These constraints reflect the radiologists’ behavior in the sense that only regions containing vessels, or at higher risk for aneurysms are scanned, while the rest of the brain is neglected. The ablation study described in section 3.1 and the FROC analysis showed that the anatomically-informed model statistically outperforms the baseline. We believe this general principle of injecting prior anatomical knowledge in the pipeline is also applicable to other pathologies with sparse spatial extent.

The state-of-the-art for automated brain aneurysm detection in TOF-MRA has been rapidly advancing in the last five years, especially due to the advent of deep learning algorithms. However, further multi-site validation is needed before safely applying these algorithms during routine clinical practice.

Although (Joo et al., 2020; Ueda et al., 2019) did publish results obtained from multiple institutions, none of them released their dataset publicly which makes comparisons between algorithms unfeasible. By openly releasing our dataset, we aim to bridge this data availability gap and foster reproducibility in the medical imaging community. The combination of our in-house dataset and the ADAM dataset will allow researchers to assess the realistic robustness of proposed algorithms on heterogeneous data generated from different scanners, acquisition protocols and study population. In addition, it could help increasing detection performances which are too still far from being clinically useful, considering that even the team with highest sensitivity on the ADAM test set (team *xlim*) only reaches a value of 70% (i.e., 30% of aneurysms still not detected), with 4 FPs per case.

In a separate analysis, we also computed the sensitivity of our model with respect to the PHASES score risk of rupture, location, and size. No significant differences were found across the three groups indicating that our model is robust to different aneurysm types.

Our work has several limitations. First, even combining our in-house dataset with the ADAM dataset, the number of subjects is still limited when compared to some related TOF-MRA (Joo et al., 2020; Ueda et al., 2019) or Computed Tomography Angiography (Park et al., 2019; Shi et al., 2020; J. Yang et al., 2020) studies. Second, we acknowledge that the number of patients for whom we compared the different annotations schemes (i.e., weak vs. voxel-wise) is limited (N=38); it is possible that statistically significant performance differences could be found with a larger sample size. Third, we have to further increase detection performances if we plan to deploy our model as a second reader for radiologists, especially to detect tiny aneurysms which are more frequently overlooked (Keedy Alexander, 2006).

In future works, we aim at enlarging the TOF-MRA dataset and experiment new variants of the 3D encoding-decoding UNET. For instance, we might consider a multi-scale approach with patches of larger (or smaller) scales. Alternatively, we are considering combining our anatomically-driven approach with the novel nnUnet model (Isensee et al., 2021) which has proven to be effective not only for aneurysm detection (it was adopted by 2 of the top-performing teams in the ADAM challenge), but also for several other segmentation tasks. We believe this combination holds promising potential to boost detection performances. Last, we plan to conduct further error analyses to identify common patterns for both false positive and false negative cases.

In conclusion, our study presented an anatomically-informed 3D UNET that tackles brain aneurysm detection across different sites. The combination of time-saving weak labels and anatomical prior knowledge allowed us to build a robust deep learning model. We believe our approach and dataset (both openly available) can foster the development of clinically applicable automated systems for the task at hand.

References

- Abousamra, S., Fassler, D., Hou, L., Zhang, Y., Gupta, R., Kurc, T., ... Chen, C. (2020). Weakly-Supervised Deep Stain Decomposition for Multiplex IHC Images. In *Proceedings - International Symposium on Biomedical Imaging* (Vol. 2020-April, pp. 481–485). <https://doi.org/10.1109/ISBI45749.2020.9098652>
- Akiba, T., Sano, S., Yanase, T., Ohta, T., & Koyama, M. (2019). Optuna: A Next-generation Hyperparameter Optimization Framework. In *Proceedings of the ACM SIGKDD International Conference on Knowledge Discovery and Data Mining* (pp. 2623–2631). Association for Computing Machinery. <https://doi.org/10.1145/3292500.3330701>
- Arimura, H., Li, Q., Korogi, Y., Hirai, T., & Abe, H. (2004). Automated Computerized Scheme for Detection of Unruptured Intracranial Aneurysms in Three- Dimensional Magnetic Resonance Angiography 1. *Academic Radiology*, 1093–1104. <https://doi.org/10.1016/j.acra.2004.07.011>
- Avants, B. B., Tustison, N., & Johnson, H. (2014). Advanced Normalization Tools (ANTs). Retrieved from <https://brianavants.wordpress.com/2012/04/13/updated-ants-compile-instructions-april-12-2012/>
- Bengio, Y., Goodfellow, I., & Courville, A. (2016). *Deep Learning*. MIT Press (Vol. 29).
- Brown, R. D., & Broderick, J. P. (2014). Unruptured intracranial aneurysms: Epidemiology, natural history, management options, and familial screening. *The Lancet Neurology*, 13(4), 393–404. [https://doi.org/10.1016/S1474-4422\(14\)70015-8](https://doi.org/10.1016/S1474-4422(14)70015-8)
- Chakraborty, D. P., & Berbaum, K. S. (2004). Observer studies involving detection and localization: Modeling, analysis, and validation. In *Medical Physics* (Vol. 31, pp. 2313–2330). John Wiley and Sons Ltd. <https://doi.org/10.1118/1.1769352>
- Chen, X., Liu, Y., Tong, H., Dong, Y., Ma, D., Xu, L., & Yang, C. (2018). Meta-analysis of computed tomography angiography versus magnetic resonance angiography for intracranial aneurysm. *Medicine (United States)*, 97(20). <https://doi.org/10.1097/MD.0000000000010771>
- Dai, X., Huang, L., Qian, Y., Xia, S., Chong, W., Liu, J., ... Ou, C. (2020). Deep learning for automated cerebral aneurysm detection on computed tomography images. *International Journal of Computer Assisted Radiology and Surgery*, 15(4), 715–723. <https://doi.org/10.1007/s11548-020-02121-2>
- Di Noto, T., Marie, G., Tourbier, S., Alemán-Gómez, Y., Saliou, G., Cuadra, M. B., ... Richiardi, J. (2020). An anatomically-informed 3D CNN for brain aneurysm classification with weak labels. In *Machine Learning in Clinical Neuroimaging and Radiogenomics in Neuro-oncology*. Retrieved from <http://arxiv.org/abs/2012.08645>
- Duan, H., Huang, Y., Liu, L., Dai, H., Chen, L., & Zhou, L. (2019). Automatic detection on intracranial aneurysm from digital subtraction angiography with cascade convolutional neural networks. *BioMedical Engineering Online*, 18(1). <https://doi.org/10.1186/s12938-019-0726-2>
- Ezhov, Zakirov, & Gusarev. (2018). Coarse-to-fine volumetric segmentation of teeth in cone-beam CT. *ArXiv*, 0–4.
- Frösen, J., Tulamo, R., Paetau, A., Laaksamo, E., Korja, M., Laakso, A., ... Hernesniemi, J. (2012). Saccular intracranial aneurysm: Pathology and mechanisms. *Acta Neuropathologica*, 123(6), 773–786. <https://doi.org/10.1007/s00401-011->

- Glorot, X., & Bengio, Y. (2010). Understanding the difficulty of training deep feedforward neural networks. *Journal of Machine Learning Research*, 9, 249–256.
- Gorgolewski, K. J. (2008). The brain imaging data structure, a format for organizing and describing outputs of neuroimaging experiments. *Scientific Data*, 208–208. https://doi.org/10.1007/978-1-4020-6754-9_1720
- Greving, J. P., Wermer, M. J. H., Brown, R. D., Morita, A., Juvela, S., Yonekura, M., ... Algra, A. (2014). Development of the PHASES score for prediction of risk of rupture of intracranial aneurysms: A pooled analysis of six prospective cohort studies. *The Lancet Neurology*, 13(1), 59–66. [https://doi.org/10.1016/S1474-4422\(13\)70263-1](https://doi.org/10.1016/S1474-4422(13)70263-1)
- Hainc, N., Mannil, M., Anagnostakou, V., Alkadhi, H., Blüthgen, C., Wacht, L., ... Winklhofer, S. (2020). Deep learning based detection of intracranial aneurysms on digital subtraction angiography: A feasibility study. *Neuroradiology Journal*, 33(4), 311–317. <https://doi.org/10.1177/1971400920937647>
- Ioffe, S., & Szegedy, C. (2015). Batch Normalization: Accelerating Deep Network Training by Reducing Internal Covariate Shift. *International Conference on Machine Learning*.
- Isensee, F., Jaeger, P. F., Kohl, S. A. A., Petersen, J., & Maier-Hein, K. H. (2021). nnU-Net: a self-configuring method for deep learning-based biomedical image segmentation. *Nature Methods*, 18(2), 203–211. <https://doi.org/10.1038/s41592-020-01008-z>
- Joo, B., Ahn, S. S., Yoon, P. H., Bae, S., Sohn, B., Lee, Y. E., ... Lee, S. K. (2020). A deep learning algorithm may automate intracranial aneurysm detection on MR angiography with high diagnostic performance. *European Radiology*, 30(11), 5785–5793. <https://doi.org/10.1007/s00330-020-06966-8>
- Ke, R., Bugeau, A., Papadakis, N., Schuetz, P., & Schönlieb, C.-B. (2020). Learning to Segment Microscopy Images with Lazy Labels. *ArXiv*, 411–428. https://doi.org/10.1007/978-3-030-66415-2_27
- Keedy Alexander. (2006). An overview of intracranial aneurysms. *McGill Journal of Medicine*.
- Kingma, D. P., & Ba, J. L. (2015). Adam: A method for stochastic optimization. *3rd International Conference on Learning Representations, ICLR 2015 - Conference Track Proceedings*, 1–15.
- Liu, X., Feng, J., Wu, Z., Neo, Z., Zhu, C., Zhang, P., ... Li, Y. (2021). Deep neural network-based detection and segmentation of intracranial aneurysms on 3D rotational DSA. *Interventional Neuroradiology*. <https://doi.org/10.1177/15910199211000956>
- Markiewicz, C. J., Gorgolewski, K. J., Feingold, F., Blair, R., Halchenko, Y. O., Miller, E., ... Poldrack, R. A. (2021). OpenNeuro: An open resource for sharing of neuroimaging data. *BioRxiv*. <https://doi.org/10.1101/2021.06.28.450168>
- McHugh, M. L. (2012). The Chi-square test of independence. *Biochemia Medica*, 23(2), 143–149. <https://doi.org/10.11613/BM.2013.018>
- Mouches, P., & Forkert, N. D. (2014). A statistical atlas of cerebral arteries generated using multi-center MRA datasets from healthy subjects. *Scientific Data*, 6(1), 1–8. <https://doi.org/10.1038/s41597-019-0034-5>
- Nakao, T., Hanaoka, S., Nomura, Y., Sato, I., Nemoto, M., Miki, S., ... Abe, O. (2018). Deep neural network-based

- computer-assisted detection of cerebral aneurysms in MR angiography. *Journal of Magnetic Resonance Imaging*, 47(4), 948–953. <https://doi.org/10.1002/jmri.25842>
- Özgün, Ç., Abdulkadir, A., Lienkamp, S., Brox, T., & Ronneberg, O. (2016). 3D U-Net: learning dense volumetric segmentation from sparse annotation. *ArXiv*, 424–432. <https://doi.org/10.1007/978-3-319-46723-8>
- Park, A., Chute, C., Rajpurkar, P., Lou, J., Ball, R. L., Shpanskaya, K., ... Yeom, K. W. (2019). Deep Learning-Assisted Diagnosis of Cerebral Aneurysms Using the HeadXNet Model. *JAMA Network Open*, 2(6), e195600. <https://doi.org/10.1001/jamanetworkopen.2019.5600>
- Rao, B., Zohrabian, V., Cedeno, P., Saha, A., Pahade, J., & Davis, M. A. (2021). Utility of Artificial Intelligence Tool as a Prospective Radiology Peer Reviewer — Detection of Unreported Intracranial Hemorrhage. *Academic Radiology*, 28(1), 85–93. <https://doi.org/10.1016/j.acra.2020.01.035>
- Razzak, M. I., Naz, S., & Zaib, A. (2018). Deep learning for medical image processing: Overview, challenges and the future. *Lecture Notes in Computational Vision and Biomechanics*, 26, 323–350. https://doi.org/10.1007/978-3-319-65981-7_12
- Shi, Z., Miao, C., Schoepf, U. J., Savage, R. H., Dargis, D. M., Pan, C., ... Zhang, L. J. (2020). A clinically applicable deep-learning model for detecting intracranial aneurysm in computed tomography angiography images. *Nature Communications*. <https://doi.org/10.1038/s41467-020-19527-w>
- Sichtermann, T., Faron, A., Sijben, R., Teichert, N., Freiherr, J., & Wiesmann, M. (2019). Deep Learning – Based Detection of Intracranial Aneurysms in 3D TOF-MRA. *American Journal of Neuroradiology*, 25–32. <https://doi.org/10.3174/ajnr.A5911>
- Smith, S. M. (2002). Fast robust automated brain extraction. *Human Brain Mapping*, 17(3), 143–155. <https://doi.org/10.1002/hbm.10062>
- Stember, J. N., Chang, P., Stember, D. M., Liu, M., Grinband, J., Filippi, C. G., ... Jambawalikar, S. (2019). Convolutional Neural Networks for the Detection and Measurement of Cerebral Aneurysms on Magnetic Resonance Angiography. *Journal of Digital Imaging*, 32(5), 808–815. <https://doi.org/10.1007/s10278-018-0162-z>
- Taghanaki, S. A., Zheng, Y., Kevin Zhou, S., Georgescu, B., Sharma, P., Xu, D., ... Hamarneh, G. (2019). Combo loss: Handling input and output imbalance in multi-organ segmentation. *Computerized Medical Imaging and Graphics*, 75, 24–33. <https://doi.org/10.1016/j.compmedimag.2019.04.005>
- Timmins, K. M., van der Schaaf, I. C., Bennink, E., Ruigrok, Y. M., An, X., Baumgartner, M., ... Kuijf, H. J. (2021). Comparing methods of detecting and segmenting unruptured intracranial aneurysms on TOF-MRAS: The ADAM challenge. *NeuroImage*, 238, 118216. <https://doi.org/10.1016/j.neuroimage.2021.118216>
- Tustison, N. J., Avants, B. B., Cook, P. A., Zheng, Y., Egan, A., Yushkevich, P. A., & Gee, J. C. (2010). N4ITK: Improved N3 bias correction. *IEEE Transactions on Medical Imaging*, 29(6), 1310–1320. <https://doi.org/10.1109/TMI.2010.2046908>
- Ueda, D., Doishita, S., & Choppin, A. (2019). Deep Learning for MR Angiography : Automated Detection of Cerebral

Aneurysms. *Radiology*. <https://doi.org/10.1148/radiol.2018180901>

Ward, J., Naik, K. S., Guthrie, F. J. A., Wilson, D., & Robinson, P. J. (1999). Hepatic Lesion Detection: Comparison of MR Imaging after the Administration of Superparamagnetic Iron Oxide with Dual-Phase CT by Using Alternative-Free Response Receiver Operating Characteristic Analysis 1. *Radiology*.

<https://doi.org/10.1148/radiology.210.2.r99fe05459>

Yang, J., Xie, M., Hu, C., Alwalid, O., Xu, Y., Liu, J., ... Long, X. (2020). Deep learning for detecting cerebral aneurysms with CT angiography. *Radiology*, 298(1), 155–163. <https://doi.org/10.1148/RADIOL.2020192154>

Yang, X., Blezek, D. J., Cheng, L. T. E., Ryan, W. J., Kallmes, D. F., & Erickson, B. J. (2011). Computer-aided detection of intracranial aneurysms in MR angiography. *Journal of Digital Imaging*, 24(1), 86–95. <https://doi.org/10.1007/s10278-009-9254-0>

Yushkevich, P. A., Piven, J., Hazlett, H. C., Smith, R. G., Ho, S., Gee, J. C., & Gerig, G. (2006). User-guided 3D active contour segmentation of anatomical structures: Significantly improved efficiency and reliability. *NeuroImage*, 31(3), 1116–1128. <https://doi.org/10.1016/j.neuroimage.2006.01.015>

Supplementary Material

Table 1: MR acquisition parameters of TOF-MRA scans of our study sample.

# scans	Vendor	Model	Field strength [T]	TR [ms]	TE [ms]	Voxel spacing [mm ³]
71	Philips	Intera	3.0	18.3	3.40	0.39 x 0.39 x 0.55
23	Siemens Healthineers	Aera	1.5	24.0	7.0	0.35 x 0.35 x 0.5
49	Siemens Healthineers	Skyra	3.0	21.0	3.43	0.27 x 0.27 x 0.5
34	Siemens Healthineers	Symphony	1.5	39.0	5.02	0.39 x 0.39 x 1
42	Siemens Healthineers	TrioTim	3.0	23.0	4.18	0.46 x 0.46 x 0.69
65	Siemens Healthineers	Verio	3.0	22.0	3.95	0.46 x 0.46 x 0.7
12	Siemens Healthineers	Prisma	3.0	20.0	3.3	0.28 x 0.28 x 0.65

Table 2. List of anatomical landmark points and corresponding locations. ACOM = Anterior Communicating Artery; Pcom = Posterior communicating artery. MCA = Middle Cerebral Artery.

Landmark point	Location
1	ACOM
2	Pcom right
3	Pcom left
4	Pericallosal proximal
5	Pericallosal distal
6	Carotid tip right
7	Carotid tip left
8	MCA right
9	MCA left
10	Basilar tip
11	Carotid extra right
12	Carotid extra left

13	Ophthalmic right
14	Ophthalmic left
15	Intradural carotid right
16	Intradural carotid left
17	MCA right distal
18	MCA left distal
19	Posterior cerebral right
20	Posterior cerebral left

A. Vessel atlas registration

We first registered the probabilistic vessel atlas to a structural anatomical scan of each patient (either T1- or T2-weighted) through a non-rigid registration (rigid + affine + symmetric normalization). Then, we registered the obtained warped volume to the TOF-MRA subject space through an affine registration.

B. Intensity criteria for negative patch sampling and sliding-window approach

Both in the negative patch sampling and in the sliding-window approach, the patches need to fulfill 4 intensity criteria. In the negative patch sampling these intensity criteria serve to extract negative training patches which are comparable to the positive ones in terms of average intensity. Similarly, in the sliding-window approach, the criteria serve to retain only the candidate patches which have an average intensity comparable to the positive patches, thus discarding all the patches that do not contain vessels.

The following four criteria were chosen by looking at the intensities of positive patches (since we want to simulate their intensity):

- 1) the ratio $\frac{\text{mean patch intensity}}{\text{max patch intensity}}$ of the 3D TOF-MRA patch must be $> 5^{\text{th}}$ percentile of the distribution of same ratios from positive patches (in-house + train ADAM). This condition ensures that the patch is locally bright enough.

- 2) the ratio $\frac{\text{mean patch intensity}}{\text{max volume intensity}}$ of the 3D TOF-MRA patch must be $> 5^{\text{th}}$ percentile of the distribution of same ratios from positive patches (in-house + train ADAM). With *volume* we mean the whole TOF-MRA volume of the patient. This condition ensures that the patch is globally bright enough.
- 3) the ratio $\frac{\text{mean patch intensity}}{\text{max patch intensity}}$ of the 3D (co-registered) vessel atlas patch must be $> 5^{\text{th}}$ percentile of the distribution of same ratios from positive patches (in-house + train ADAM). This condition ensures that the co-registered vessel atlas is non-empty for this patch, and thus the patch likely contains a vessel.
- 4) the ratio $\frac{\text{mean patch intensity}}{\text{max volume intensity}}$ of the 3D (co-registered) vessel atlas patch must be $> 5^{\text{th}}$ percentile of the distribution of same ratios from positive patches (in-house + train ADAM). With *volume* we mean the whole vessel atlas co-registered to subject space. Again, this condition ensures that the patch is globally bright.

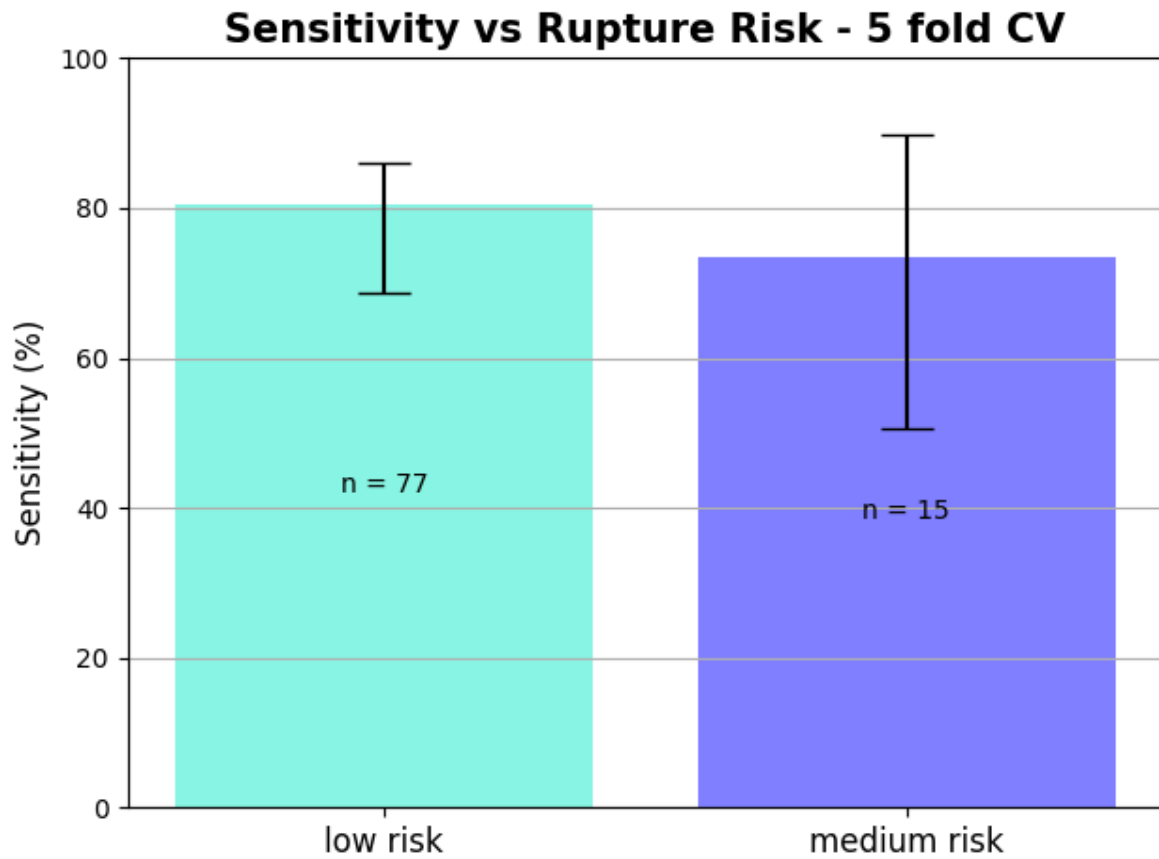
We always choose the conservative 5^{th} percentile of the distributions to ensure that the four conditions are extremely loose.

C. Sliding-window approach

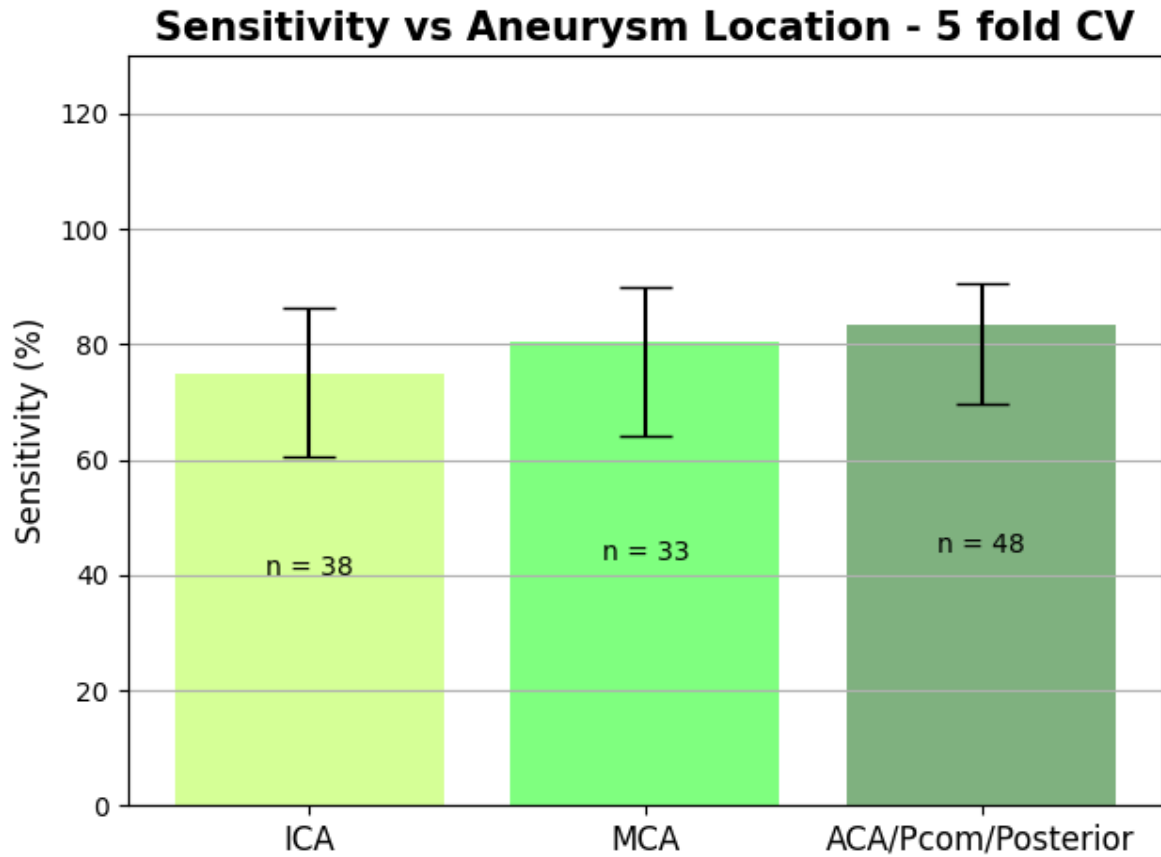
Every test volume is explored with neighboring, overlapping patches. Each patch is fed to the trained network that outputs the corresponding semantic segmentation. The probabilistic segmentations are then binarized. Once the volume has been fully explored, all the binarized predictions are merged back to re-create the output volume. In this work, we used an overlap of 50% in all directions and we averaged overlapping predictions.

D. Weak label creation for 38 subjects with voxel-wise labels

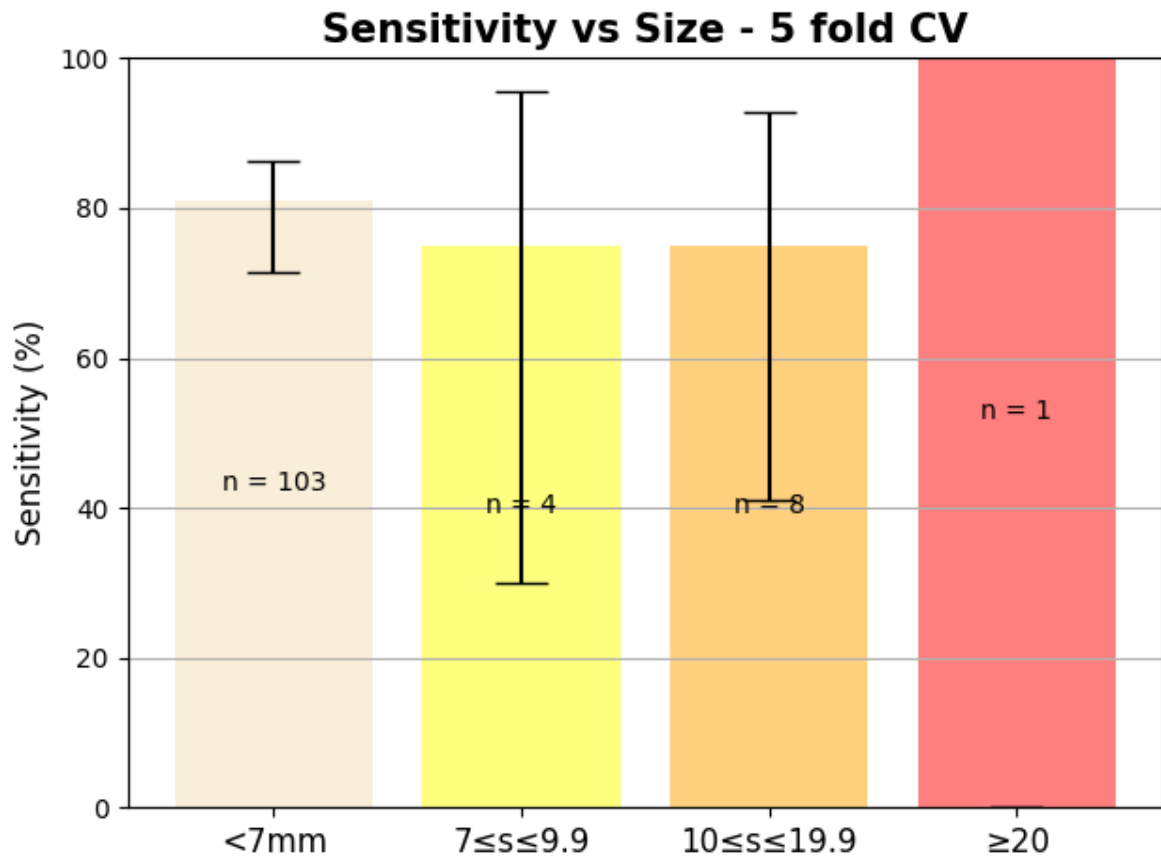
For the 38 subjects with voxel-wise labels, we created corresponding artificial weak labels. In other words, we converted the slice-by-slice annotations into spheres (we “*weakened*” the voxel-wise labels). The center of each artificial sphere corresponds to the center-of-mass of the corresponding voxel-wise label, while the diameter of the sphere corresponds to the maximum diameter of the voxel-wise label.



Supplementary Fig 1. Sensitivity of our anatomically-informed 3D-UNET across the test folds with respect to the two risk-of-rupture groups. The *low-risk* group indicates aneurysms that will be monitored through imaging, but do not require any intervention. The *medium-risk* group includes more dangerous aneurysms that can be considered for treatment. Bar plots indicate the mean sensitivity value; error bars represent the 95% Wilson score interval. CV = cross-validation. n = number of sensitivity values in the distribution.



Supplementary Fig 2. Sensitivity of our anatomically-informed 3D-UNET across the test folds with respect to the PHASES score aneurysm locations. ICA = Internal Carotid Artery, MCA = Middle Cerebral Artery, ACA = Anterior Cerebral Arteries, Pcom = Posterior communicating artery, Posterior = posterior circulation. Bar plots indicate the mean sensitivity value; error bars represent the 95% Wilson score interval. CV = cross-validation. n = number of sensitivity values in the distribution.



Supplementary Fig 3. Sensitivity of our anatomically-informed 3D-UNET across the test folds with respect to the PHASES score sizes in mm. Bar plots indicate the mean sensitivity value; error bars represent the 95% Wilson score interval. CV = cross-validation. n = number of sensitivity values in the distribution.